Influence of the Substrate and Precursor on the Magnetic and Magneto-transport Properties in Magnetite Films

Enio Lima Jr.[a,1], Giancarlo E. S. Brito[b], Christian Cavelius[c], Vladimir Sivakov[c], Hao Shen[c], Sanjay Mathur[c] and Gerardo F. Goya[d]

[a]*CONICET, Centro Atómico Bariloche, 8400 S. C. de Bariloche, RN, Argentina;* [b]*Universidade de São Paulo, Instituto de Física, CP 66318, São Paulo, BR-05315970 Brazil;* [c]*Leibniz Inst. New Mat., CVD Division, Saarbrucken, D-66123 Germany;* [d]*Instituto de Nanociencia de Aragon (INA), University of Zaragoza, Spain.*

Abstract: We have investigated the magnetic and transport properties of nanoscaled Fe_3O_4 films obtained from Chemical Vapor Deposition (CVD) technique using $[Fe^{II}Fe_2^{III}(OBu^t)_8]$ and $[Fe_2^{III}(OBu^t)_6]$ precursors. Samples were deposited on different substrates (*i.e.*, MgO (001), $MgAl_2O_4$ (001) and Al_2O_3 (0001)) with thicknesses varying from 50 to 350 nm. Atomic Force Microscopy analysis indicated a granular nature of the samples, irrespective of the synthesis conditions (precursor and deposition temperature, T_{pre}) and substrate. Despite the similar morphology of the films, magnetic and transport properties were found to depend on the precursor used for deposition. Using $[Fe^{II}Fe_2^{III}(OBu^t)_8]$ as precursor resulted in lower resistivity, higher M_S and a sharper magnetization decrease at the Verwey transition (T_V). The temperature dependence of resistivity was found to depend on the precursor and T_{pre}. We found that the transport is dominated by the density of antiferromagnetic antiphase boundaries (AF-APB's) when $[Fe^{II}Fe_2^{III}(OBu^t)_8]$ precursor and $T_{pre} = 363$ K are used. On the other hand, grain boundary-scattering seems to be the main mechanism when $[Fe_2^{III}(OBu^t)_6]$ is used. The Magnetoresistance (MR(H)) displayed an approximate linear behavior in the high field regime ($H > 796$ kA/m), with a maximum value at room-temperature of ~ 2-3 % for $H = 1592$ kA/m, irrespective from the transport mechanism.

Keywords: Magnetite films, chemical vapor deposition, magnetoresistance, anti-phase boundaries.

1. INTRODUCTION

Magnetite (Fe_3O_4) is a ferrimagnet below its Curie temperature $T_C = 850$ K, having an inverse spinel cubic structure with O_{h7} (Fd3m) space group [1]. The Fe ions are distributed among two different crystallographic sites: the octahedral B site occupied by both Fe^{2+} and Fe^{3+} ions, and the tetrahedral A site, where only Fe^{3+} ions are present. Previous works on band calculations in bulk magnetite have shown that only one of the spins channels has a gap at the Fermi level, suggesting that conduction electrons are fully spin-polarized in Fe_3O_4 [2]. In spite of the fact that this theoretical polarized band structure should display a large magnetoresistance (MR) effect, this consequence has not yet been observed experimentally. Indeed, only a modest MR effect has been so far observed at room temperature (up to 3-4 % in fields of 1592 kA/m) for thin films, whereas for high-quality Fe_3O_4 single crystals the MR effect is absent [3-6].

Fe_3O_4 films show divergences regarding the magnetic behavior as compared with bulk material. For example, Arora *et al.,* [7] have observed that saturation magnetization of epitaxial films is strongly related to the thickness of the film, obtaining an M_S value of 1000 kA/m for 5 nm in comparison to the 512 kA/m of the bulk material [8]. Saturation field of epitaxial or polycrystalline films (up to 1194 kA/m) exceeds by far the corresponding value for single crystals (~ 24 kA/m) [9]; however, the experimental values on MgO obtained for the effective magnetic anisotropy on these films have explained assuming only magnetocrystalline and shape anisotropies, without any additional mechanism [10].

There are at present no general consensus regarding the detailed magnetic structure of Fe_3O_4 epitaxial films obtained from different synthesis routes such as molecular beam epitaxy (MBE), pulsed laser deposition (PLD) *etc.*, and also related to different substrates such as MgO, Al_2O_3, $MgAl_2O_4$, $BaTiO_3$ and $SrTiO_3$ [7,9-16], despite some results indicates that the magnetism and magneto-transport phenomena in this kind of film are controlled by the domain boundaries and the anti-ferromagnetic couple strength in the boundary [9]. For example, the close structural match between MgO and Fe_3O_4 cell parameters (about 0.3 %) usually yields to epitaxial growth on this substrate. However, it has been demonstrated that the lower symmetry and larger unit cell of the magnetite crystal structure can result in 'broken' cation sublattices at the Fe_3O_4 layers on MgO, as well as different directions on nucleation of Fe_3O_4 islands on the first stages of the growth process [10]. These considerations have been the basis of one of the key concepts to understand the magnetotransport properties of Fe_3O_4 epitaxial films through the antiphase boundary (APB). The APB is a natural growth defect in epitaxial films, whose origin is associated to discontinuities in the cation B sublattice, along definite directions on the angle and distances governing the A-A, B-B, and A-B exchange interactions. The magnetic coupling over a large fraction of these APB´s is antiferromagnetic (AF), yielding a local magnetic structure different than the bulk material [17]. It has been proposed that these AF-APBs are efficient scattering centers for the fully spin-polarized electrons that results in the increased resistance observed in thin films. The domain size or the APB density seems to be dependent of the thickness [17] and of the misfit with the structure of the substrate [15].

Polycrystalline Fe_3O_4 films were prepared by sputtering, chemical vapor deposition (CVD), PLD, electrodeposition, etc, on different substrates ($MgAl_2O_4$, Al_2O_3, quartz, glass, SiO, etc.) [9, 18-20]. The structure and the granulometry for these films depends strongly from the synthesis method and growth conditions, as well as from the substrate. In this way, the magnetic and transport properties are strongly influenced by the synthesis method and growth conditions. In general, polycrystalline films present high saturation field as consequence of the grain boundary, and its value depend on the morphology, stoichiometry and structure of the film [9, 18]. Resistivity is higher than the bulk one, as consequence of the scattering in the grain boundaries [9, 18]. Magneto-resistive behavior are also observed for polycrystalline films and it is determined by the spin-polarized electron tunneling trough the grain boundary [9, 18]. Magnetic and transport properties of Fe_3O_4 films are also de-

---

*Address correspondence to this author at the CONICET, Centro Atómico Bariloche, 8400 S. C. de Bariloche, RN, Argentina; Tel: (54) 294 4445158; Fax: (54) 294 4445299; E-mail: lima@cab.cnea.gov.ar

pendent of crystallinity and stoichiometric characteristics, which are associated to the growth conditions too. For example, Bohra *et al* [19] have observed significant improves in the crystallinity and in the magnetic properties of annealed polycrystalline films, while Mantovan *et al.,* [18] correlate the number of vacancies and the stoichiometric characteristics with the magnetic and transport properties of the system.

From the above discussion it is clear that precise control over the morphology and phase purity is necessary to disentangle the underlying transport mechanisms, inasmuch as they depend strongly dependent on their chemical composition and microstructure. In this context, CVD processes using single molecular precursors offers a convenient method for the size- and morphology-controlled deposition of metal oxide film [21, 22]. Molecular chemical compounds that mimic the atomic composition or bonding features of solid phases are attractive precursors because they allow a control over the evolution of materials from discrete single- or poly-atomic units (molecule) to the extended frameworks (bulk) [23-25]. From this, we can obtain a molecular design for conservation of valence and stoichiometry in CVD deposited Magnetite films. The mixed-valent iron alkoxide $[Fe^{II}Fe_2^{III}(OBu^t)_8]$ is a precursor that contains both Fe(II) and Fe(III) centers in a single framework. Thus, it is expected that it governs the formation of Fe_3O_4 by imposing a positional control on phase-building ions.

In this work, we have investigate the magnetic and magneto-transport properties of Fe_3O_4 films deposited by CVD with using two distinct precursors: $[Fe^{II}Fe_2^{III}(OBu^t)_8]$ and $[Fe_2^{III}(OBu^t)_6]$. The films were deposited in three different substrates ($MgO(001)$, $MgAl_2O_4$ (001) and Al_2O_3 (0001)). We have observed a strong and straight influence of the precursor on the magnetic and transport properties of Fe_3O_4 films, overlapping the influence of the mismatch between the structure of films and the substrates. These results are important for future application of precursors with molecular design for conservation of valence and stoichiometry for CVD-deposited Magnetite films.

2. MATERIALS AND METHODS

The molecular framework of the $[Fe^{II}Fe_2^{III}(OBu^t)_8]$ is formally constituted by a Fe^{II} cation coordinated by two bidentate $\{Fe^{III}(OBu^t)_4\}^{-1}$ anions. All the iron atoms are present in a distorted tetrahedral environment of oxygen. This compound represents mixed-valent iron alkoxide mimicking the features of a mixed-valent condensed phase. $[Fe^{II}Fe_2^{III}(OBu^t)_8]$ is volatile and can be transferred intact in the vapor phase at $263 \ K/10^{-3}$ Torr. The films properties of the films deposited from this precursor are compared with those deposited from the precursor $[Fe^{III}_2(OBu^t)_6]$, that contains only Fe^{III} ions.

A total of nine Fe_3O_4 films were synthesized in a cold-wall Chemical Vapor Deposition (CVD) reactor using the iron alkoxide precursors as a single-source for Fe^{II} and Fe^{III} ions. The series was composed of three sets of three crystalline films deposited on (001) oriented MgO (mismatch ~0.3 %) and $MgAl_2O_4$ (mismatch ~3.9 %), as well as on (0001) oriented Al_2O_3 (mismatch ~8%). Each of these three sets were obtained for different synthesis conditions (systematically changing the temperature of the precursor $T_{pre} = 354 - 363 \ K$, and deposition time), and using $[Fe^{III}_2Fe^{II}(OBu^t)_8]$ and $[Fe^{III}_2(OBu^t)_6]$ as precursors. Table **1** summarizes the information about synthesis conditions for each sample. The temperature of the substrate (T_{sub}) was maintained the same (723 K) for all samples.

To further characterize the samples, we performed Rutherford Backscattering Spectroscopy (RBS) measurements in order to extract the thickness (d) and the composition of the films. The obtained film thicknesses, d, ranged from 50 to 350 nm whereas the relative amounts of Fe and O fitted from the profiles are close to the fully stoichiometric magnetite Fe_3O_4. Information about the thickness and composition obtained from RBS analysis of each sample is given in Table **1**.

X-ray diffraction patterns were collected with θ-2θ geometry and using Ni-filtered Cu-K_α radiation (λ=0.15418 nm). The resistivity measurements as a function of temperature ($\rho(T)$) were made using a DC four-probe method. For all contacts we obtained linear

Table 1.   Synthesis Conditions and the Results from RBS and XRD Analyzes for Each Sample

Sample	Substrate	Precursor	T_{sub} (K)	T_{pre} (K)	Deposition time	RBS		
						d (nm)	Fe%	O%
S1	$MgAl_2O_4$ (100)					214	44	56
S2	MgO (100)	$Fe_3(OBu^t)_8$	723	363±2	15 min.	200	38	62
S3	Al_2O_3 (0001)					208	41	59
S4	$MgAl_2O_4$ (100)					114	41	59
S5	MgO (100)	$Fe_2(OBu^t)_6$	723	354±1	60 min.	71	44	56
S6	Al_2O_3 (0001)					50	44	56
S7	$MgAl_2O_4$ (100)					305	39	61
S8	MgO (100)	$Fe_3(OBu^t)_8$	723	357±2	15 min.	250	38	52
S9	Al_2O_3 (0001)					360	42	58

T_{sub} = temperature of the substrate; T_{pre} = temperature of the precursor; DPT = Deposition Time; d = thickness of the film obtained by RBS. Fe% and O% are the atomic mass percentage as obtained from RBS profiles.

IxV curves at room temperature applying DC voltages (V) and measuring the current (I) in a four-point geometry. Magnetization curves were made in a commercial SQUID magnetometer as function of temperature (M(T)), in zero-field-cooling (ZFC) and field-cooling (FC) modes, and applied field (M(H)) up to 5570 kA/m, with applied field parallel (in-plane) and perpendicular (out-of-plane) to the film plane. Magneto-resistance curves (MR(H)) at room temperature were collected up to 1592 kA/m using a four-probe geometry, with applied field in- and out-plane. The magneto-resistance MR(H) was calculated using the relationship:

$$MR\ (H) = (R(H) - R(0))/R(0),\qquad\qquad \text{eq. (1)}$$

where R(0) is the resistance at zero applied magnetic field. Magnetic (MFM) and Atomic force microscopy (AFM) images were made in Nanoscope III A – Digital Instruments, operating in tapping mode, and phase contrast for MFM images.

RESULTS AND DISCUSSION

Table **1** shows a difference in the deposition rate of the films depending of the precursor and T_{pre}, as calculated by the thickness from RBS analysis. The highest deposition rate were obtained for the set formed by samples S7, S8 and S9 (deposited from precursor $[Fe^{II}Fe^{III}_2(OBu^t)_8]$ at T_{pre}= 357 K), being around 16.7 – 24.0 nm/min. Close deposition rates were observed for samples S1, S2 and S3 (13.3 – 14.3 nm/min.), also deposited from precursor $[Fe^{II}Fe^{III}_2(OBu^t)_8]$, but at T_{pre}= 363 K. Finally, the set formed by samples S4, S5, and S6, which were deposited from precursor $[Fe^{III}_2(OBu^t)_6]$ at (T_{pre} = 354 K), presents the lowest deposition rates (0.8 – 1.9 nm/min.). Therefore, the deposition kinetic drastically changes with the precursor used in the process, while the effects of the temperature of the precursor T_{pre} are significantly smaller. Table **1** also gives the composition values obtained from RBS, being between 38 % and 44 % *at.* Fe for all samples. The nominal value for the bulk magnetite is ~ 42.8 % *at.* Fe.
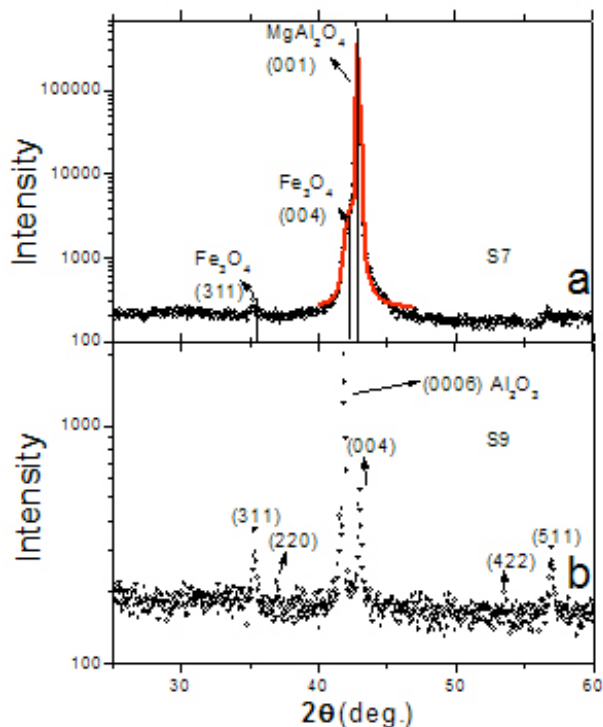

Fig. (1). X-ray diffraction (XRD) patterns of films (**a**) S7 and (**b**) S9 grown on MgAl₂O₄(001) Al₂O₃, respectively. Solid line is the fitting with 3 pseudo-Voigt curves corresponding to the peaks of Fe₃O₄ (004) direction together with K$_{a1}$ and K$_{a2}$ peaks of the (001) direction of MgAl₂O₄.

Crystallographic analysis (XRD) of sample S7 (Fig. **1a**), deposited from precursor $[Fe^{II}Fe^{III}_2(OBu^t)_8]$ at T_{pre}= 357 K, shows the peak characteristic of (004) plane of magnetite together with the intense peak corresponding to the (001) direction of the MgAl₂O₄ precursor. We also observe the peak relative to the direction (311) with very low intensity in comparison to the (004) one (about 50 times smaller). The main contribution to the XRD profile of this sample can be fitted with three pseudo-voigt curves: peak (004) of magnetite and the $K\alpha_1$ and $K\alpha_2$ contributions of the peak (001) from the substrate. Full width at half maximum (FWHM) for the Fe₃O₄ (004) peak is 0.8º against a FWHM= 0.1º for the MgAl₂O₄ (004) peak. For comparison, epitaxial films of Fe₃O₄ with roughness about 0.28 nm deposited by PLD on MgAl₂O₄ show FWHM ~ 0.2º - 0.3º for the (004) peak [26, 27] while the FWMH= 1º was observed for polycrystalline film growth by CVD on MgAl₂O₄ [18]. Similar characteristics were exhibited by the the XRD profiles of samples S8 (precursor $[Fe^{II}Fe^{III}_2(OBu^t)_8]$, T_{pre}= 357 K) and S5 (precursor $[Fe^{III}_2(OBu^t)_6]$, T_{pre}= 354 K) deposited on MgO (001). Fig. (**1b**) presents the XRD profile of sample S9, deposited on Al₂O₃ (0001), with the precursor $[Fe^{II}Fe^{III}_2(OBu^t)_8]$ and T_{pre}= 357 K, where the diffraction lines (311), (222), (004), (422) and (511) of magnetite are observed together with the diffraction line (0001) of Al₂O₃, although the magnetite peaks present distinct intensity relation when compared with that one expected for bulk material. According to this XRD analysis, the films deposited from the precursor $[Fe^{II}Fe^{III}_2(OBu^t)_8]$ are very crystalline, with the films on MgO and MgAl₂O₄ being strongly oriented in the (004) direction, while the films on Al₂O₃ present several crystalline orientations.

Fig. (**2a-c**) present the AFM images of samples deposited from both precursors on MgO (S2, S5 and S8), evidencing the granular nature of these films, with rms = 8.2, 7.9 and 4.1 nm, respectively. AFM images of samples S7 and S9, deposited from precursor $[Fe^{II}Fe^{III}_2(OBu^t)_8]$ on MgAl₂O₄ and Al₂O₃, respectively, are presented in Fig. (**2d**) and (**2e**), also showing a granular nature and rms = 8.0 and 9.5 nm, respectively.

Correlating the AFM and XRD results, all films prepared from precursor $[Fe^{II}Fe^{III}_2(OBu^t)_8]$ present a granular nature and high crystallinity, with the films growth on MgO and MgAl₂O₄ presenting a preferential growth on the (004) direction of the magnetite structure, while the film grown on Al₂O₃ does not present a preferential growth direction. These results are probably related to the structural mismatch between the Fe₃O₄ films and the different substrates: for the mismatch with MgO (0.3 %) or MgAl₂O₄ (3.9 %) is smaller than Al₂O₃ (~ 8.9 %). At the same time, AFM and XRD results indicates that the granular nature of the films and the crystallinity present no dependence with the precursor or the T_{pre} used in the deposition procedure.

3.1 - Magnetization

Fig. (**3**) presents the M(T) curves (H= 798 A/m) measured at ZFC and FC modes for all samples. The Verwey Transition (temperature of charge ordering - T_V) is clearly evidenced in all curves as a sharp drop in the magnetization for both curves. T_V was assumed as the maximum value of the ZFC derivative curve and varies between 110-118 K. The values of T_V and the width of the transition in the temperature axis (δT_V) of each sample are given in Table **2**. For comparison, we also present in Fig. (**3**) the M(T) curves of a commercial magnetite monocrystal, which shows a markedly (δT_V= 8 K) Verwey transition at T_V = 109 K. This value of T_V is lower than the expected for the magnetite (122 – 125 K), indicating a variation in the stoichiometry of the monocrystal with respect to magnetite [2]. T_V values obtained for the films are between the monocrystal and the bulk ones, at the same time, our values of δT_V are slightly higher than that one of the monocrystal. These are evidences of the stoichiometric and structural quality of our films, since T_V is strongly affected by these factors. In Fig. (**4**),
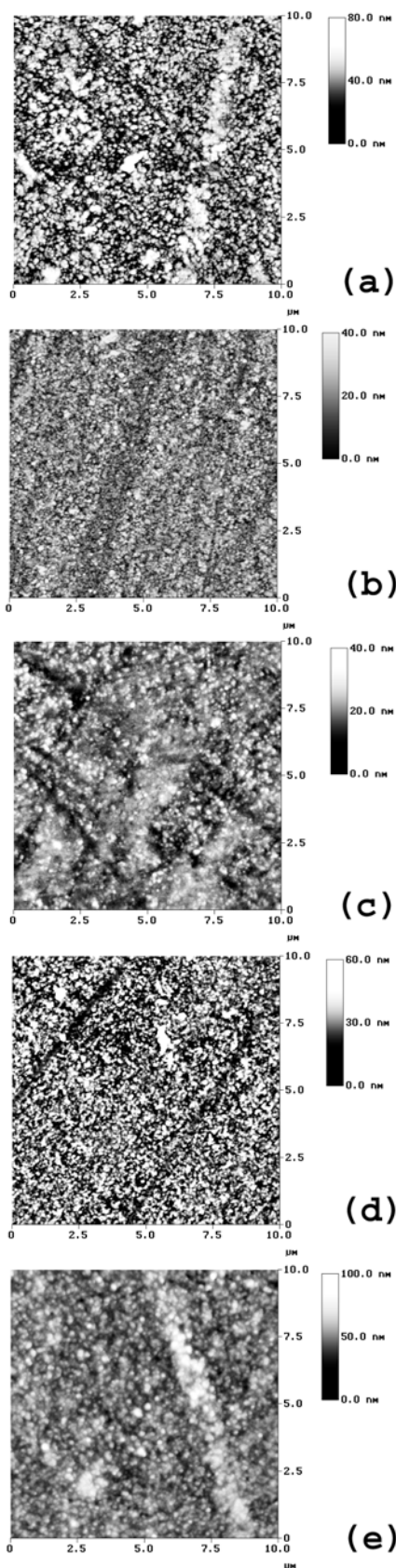
Fig. (2). AFM images of samples (**a**) S2, (**b**) S5 and (**c**) S8 grown on MgO (001) from both precursors, and Fig. (**2d**) and (**2e**) present the AFM images of samples S7 and S9, which were grown on MgAl$_2$O$_4$ and Al$_2$O$_3$, respectively, from precursor [Fe^{II}Fe$^{III}_2$(OBu^t)$_8$].
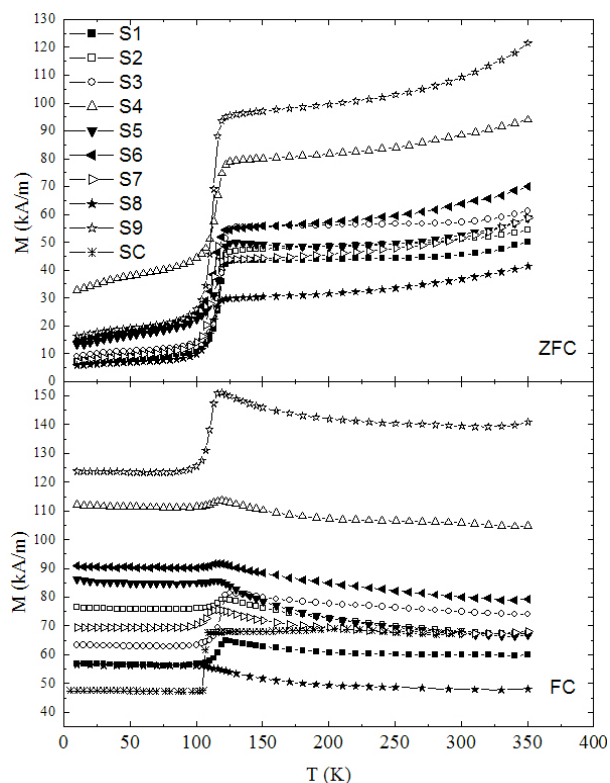

Fig. (3). M(T) curves (H = 796 kA/m) measured at ZFC and FC modes for all samples. For comparison, we also present in Fig. (**3**) the M(T) curves of a commercial magnetite monocrystal.

we present the T_V as function of the thickness, showing clearly three groups of samples: (S1, S2, S3), (S4, S5, S6) and (S7, S8, S9). These groups are reflected in the plot of δT_V *vs.* thickness (see inset of Fig. (**4**)) too, except for sample S9, closer to samples S1, S2, and S3. Therefore, there is a straight connection between the synthesis conditions (precursor and T_{pre}) and T_V and δT_V. The group (S1, S2, S3) (deposited from [Fe^{II}Fe$^{III}_2$(OBu^t)$_8$] with T_{pre} = 363 K) presents the smaller values of δT_V. Group (S7, S8, S9) have intermediate values of δT_V (same precursor with T_{pre}= 357 K), while the group (S1, S2, S3) present the highest ones (precursor [Fe$^{III}_2$(OBu^t)$_6$] and T_{pre}= 354 K).
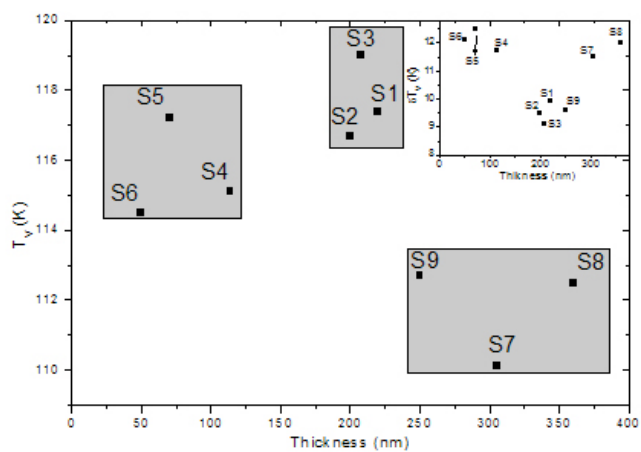

Fig. (4). Temperature of the Verwey Transition (T_V) as function of the film thickness, showing clearly three groups of samples: (S1, S2, S3), (S4, S5, S6) and (S7, S8, S9). Inset: plot of δT_V *vs.* thickness of all samples.

Table 2. **Temperature of the Verwey transition (T_V) and the width of the transition in the temperature axis (δT_V) determined from the derivative of the $M_{ZFC}(T)$ for all samples. Saturation magnetization (M_S, kA/m) for all samples obtained by extrapolating the $M(H^{-2})$ curve for $H^2 \to 0$**

Sample	S1	S2	S3	S4	S5	S6	S7	S8	S9
T_V (K)	117.7	116.6	117.9	115.0	117.9	115.0	110.9	112.9	112.9
δT_V (K)	9.9	9.5	9.1	11.7	12.5	12.1	11.5	12.0	9.6
M_S (kA/m)	519	558	530	467	460	450	518	529	530

Fig. (**5a**) shows the M(H) curves for in-plane direction of all samples measured at room temperature and the magnetization values are given in kA/m by using the volume of the film in each sample. The diamagnetic component of the corresponding substrate was subtracted from the M(H) curves. It is not observed significant differences in the coercive field $H_C = 14 - 15$ kA/m of the samples. However, it is clear a difference in the saturation magnetization (M_S). As observed in Table **2**, samples prepared from precursor [$Fe^{II}Fe^{III}_2(OBu^t)_8$] (samples S1-S3 and S7-S9) have M_S values between 518 and 558 kA/m, while samples from precursor [$Fe^{III}_2(OBu^t)_6$] (samples S4-S6) present no saturation up to 1592 kA/m, with extrapolated values given $M_S = 450 – 467$ kA/m. The absence of saturation for the fields used in our magnetization measurements is expected for polycrystalline films as consequence of the grain boundaries [28]. In-plane and out-of-plane M(H) curves of sample S5 and S8 are compared in Fig. (**5b**), showing that the in-plane in the easy direction for both (demagnetization factor was taken into account in the out-of-plane curves). This result is expected because of the shape anisotropy, with in-plane and out-of-plane curves converging one to another at $H = 398$ kA/m, which indicates the intensity of the shape anisotropy.

In spite of the same granular nature of all samples in the present series, some differences in their magnetic properties were observed in their values of M_S, saturation field, T_V and δT_V. Regarding M_S values, the highest values were observed for those samples prepared from [$Fe^{II}Fe^{III}_2(OBu^t)_8$] precursor. Concurrently, those samples were found to saturate at lower applied fields. We have previously mentioned that a direct relation between the precursor and T_{pre} with T_V and δT_V was observed. We propose that this dependence is associated to the deposition kinetics (thickness–see Fig. (**4**)): group (S1, S2, S3) (deposited from [$Fe^{II}Fe^{III}_2(OBu^t)_8$] with $T_{pre} = 363$ K) presents the smaller values of δT_V; group (S7, S8, S9) have intermediate values of δT_V (same precursor with $T_{pre}= 357$ K); and group (S1, S2, S3) (precursor [$Fe^{III}_2(OBu^t)_6$] and $T_{pre}= 354$ K) present the highest values of T_{pre} and δT_V. These results indicate that the precursor [$Fe^{II}Fe^{III}_2(OBu^t)_8$] produce samples with high magnetic quality in comparison to the precursor [$Fe^{III}_2(OBu^t)_6$], probably as consequence of the higher local crystallographic order in the samples associated to the first one, which is reflected in the values of T_{pre} and δT_V. The differences in the magnetic properties between samples prepared from the two precursors is also probably related to the differences in the deposition kinetic, as evaluated from RBS analysis (see Table **1**).

Fig. (**6a-c**) displays the AFM and MFM images side-by-side for the samples S2, S5 and S8, respectively. These images indicate that there are differences in the patterns observed in MFM images and the morphology in the respective AFM ones. For samples S2 and S8, we observe that MFM pattern seems to be smaller than the grains observed in the AFM image, while for sample S5 we observed the opposite situation: larger pattern in MFM image than in the AFM one. Thus, in the last sample, the magnetic domain proba-
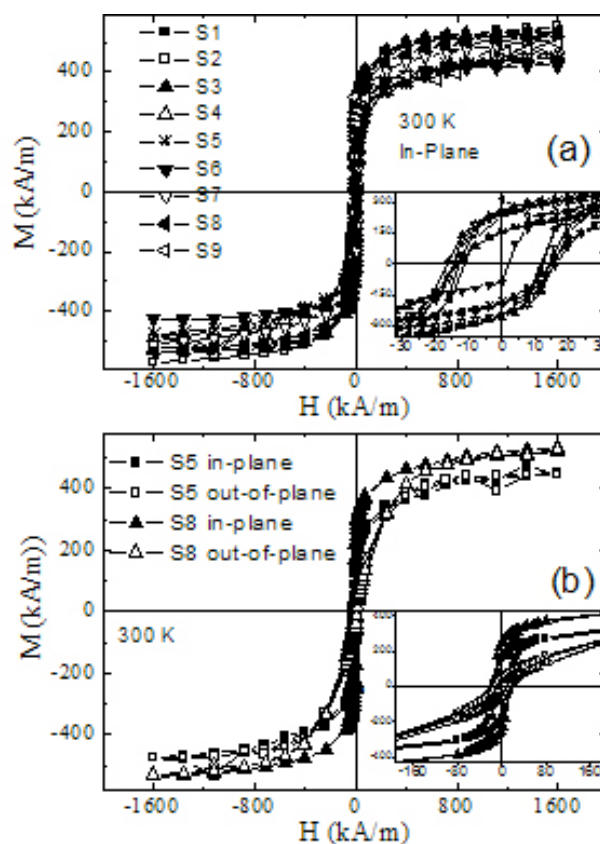

Fig. (5). Fig. (**5a**) shows the M(H) curves for in-plane direction of all samples measured at room temperature and the magnetization values are given in kA/m by using the volume of the film in each sample. Fig. (**5b**) displays the in-plane and out-of-plane M(H) curves of sample S5 and S8, showing that the in-plane is the easy direction for both (demagnetization factor was taken into account in the out-of-plane curves).

bly incorporate more than one grain and in samples S2 and S8 one grain should present more than one magnetic domain. The AFM/MFM images of samples S7 and S9 deposited on $MgAl_2O_4$ and Al_2O_3, respectively (Fig. **6d-e**), showed no major differences with sample S8 (deposited on MgO). This result demonstrates that the final magnetic structure has a stronger dependence on the precursor than on the substrate, in agreement with the results from M(T) and M(H) data.

3.2 – Transport and Magneto-Transport

The resistivity curves as function of temperature ($\rho(T)$, with 90 K < T < 300 K, excepting for samples S2, with 120 K < T < 300 K)
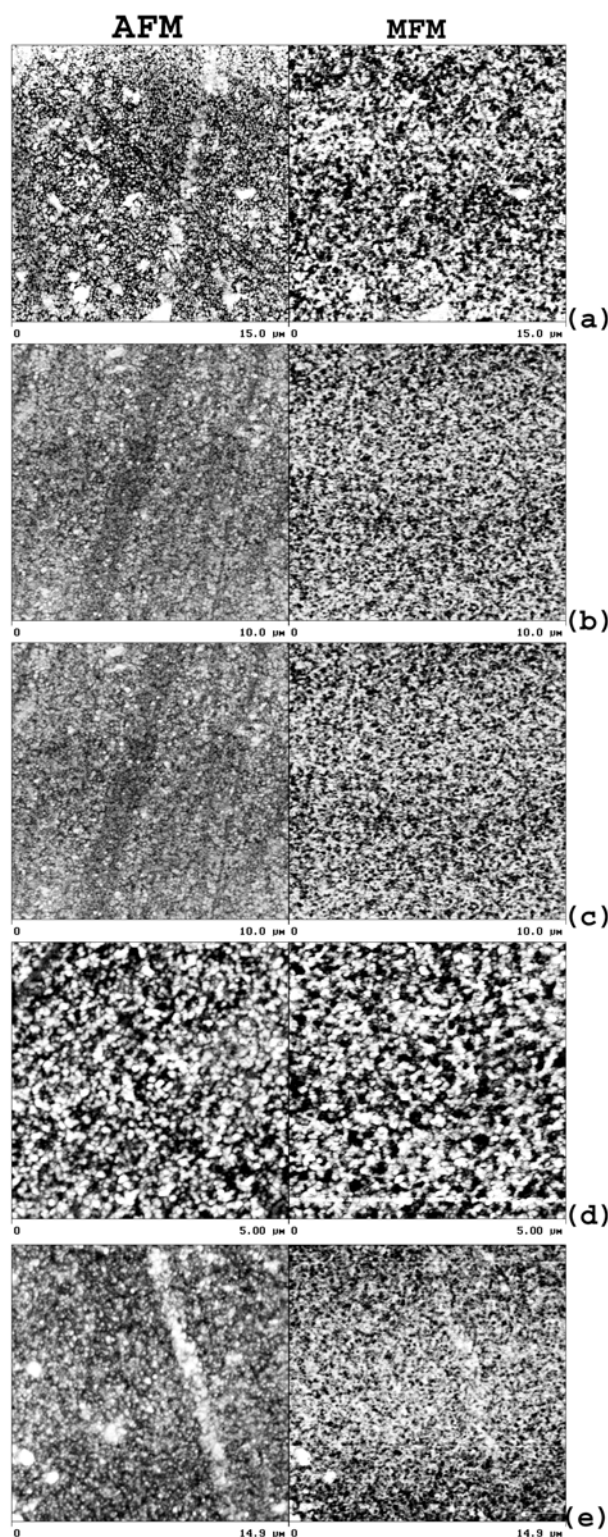
Fig. (**6**). AFM and MFM images of samples (**a**) S2, (**b**) S5 and (**c**) S8 deposited on MgO (001) using both precursors, and AFM and MFM images of samples (**d**) S7 and (**e**) S9, deposited from precursor [Fe^{II}Fe$^{III}_2$(OBu^t)$_8$] on MgAl$_2$O$_4$ and Al$_2$O$_3$, respectively.

of all samples show a continuous increase with decreasing the temperature for all samples, as expected for the magnetite. Fig. (**7a**) displays the plot of ln(ρ(T)) *vs.* 1/T for samples S1, S2 and S3 (de-

posited from precursor [Fe^{II}Fe$^{III}_2$(OBu^t)$_8$] at 363 K) and sample S8 (precursor [Fe^{II}Fe$^{III}_2$(OBu^t)$_8$] at 357 K on MgO), showing a linear behaviour and indicating a thermally-activated transport mechanism:

$$\rho(T) = \rho(0)\exp(E_a/k_B T), \qquad \text{eq. (2)}$$

where ρ_0 is the resistivity for $k_B T \gg E_a$ and E_a is the activation energy. The resistivity values of this set of samples are lower with increasing the thickness of the films. For samples S1, S3 and S8, a discontinuity is observed for $T < T_V$ as consequence of the charge ordering below the Verwey transition.

For samples S4, S5 and S6 (deposited from precursor [Fe$^{III}_2$(OBu^t)$_6$] at 354 K) ,and samples S7 and S9 (precursor precursor [Fe^{II}Fe$^{III}_2$(OBu^t)$_8$] at 357 K on MgAl$_2$O$_4$ and on Al$_2$O$_3$, respectively), the curves ln(ρ(T)) *vs.* 1/T do not present a linear behaviour, being closer to the linearity when plotted as function of 1/T$^{1/2}$ (see Fig. **7b**).

These two distinct thermal behaviours observed for the ln(ρ(T)) curves of our films indicate a difference in the fundamental mechanism of the charge transport in these systems. In a polycrystalline film, the thermal dependence of the resistivity with 1/T$^{1/2}$ is expected, since the charge transport is dominated by the scattering of grain boundaries [6, 18]. In this case, the resistivity depends majority from the grains size, which is associated preferentially to the synthesis conditions and not with the thickness of the film. In fact, we observe that samples S4, S5, S6, S7 and S9 present similar values of resistivity for all the temperature range measured, independently from the thickness of each sample.

For Samples S1, S2, S3 and S8, the linear dependence of ln(ρ(T)) *vs.* 1/T supports the thermally-activated mechanism and suggests that spin-polarized transport through the anti-phase-boundaries (APBs) is the major mechanism. Accordingly, the anti-ferromagnetic coupling of APBs [29] will act as a scattering center for the fully spin-polarized electrons. In our highly crystalline, orientated and granular films, the presence of APBs is probably associated to the correlation between the morphological (grain size) and magnetic (domain size) characteristics lengths. For samples S1, S2, S3 and S8 the domain size seems to be smaller than the crystalline one. It is expected that the APBs density decreases with increasing the film thickness [17], and therefore the resistivity should decrease for thicker films. In our samples this characteristic can be clearly observed, as pointed out in Fig. (**7b**).

From the linear fit of the data presented in Fig. (**7b**) with eq. (2), we determined the values of E_a and ρ_0 for samples S1, S2, S3 and S8 (Table **3**). As expected ρ_0 decreases with increasing the thickness, varying from 0.3×10^{-3} to 2.2×10^{-3} Ω.cm, in agreement with those ones obtained for epitaxial Fe$_3$O$_4$ films with 50 and 200 nm [17, 29]. While the value of E_a are almost constant among these samples, varying from 70 meV for sample S1 to 75 meV for sample S8, close to the values observed in the literature for epitaxial films of magnetite [2,4].

In general, the resistivity of films whose the scattering in the grain boundaries are dominant present for the polycrystalline films, where this mechanism is dominant, is larger than that of epitaxial ones [6,9,18,30]. Our results presented in Fig. (**7a**) and (**7b**) agrees with this prediction, with samples S4, S5, S6, S7 and S9 presenting a resistivity about 10 or 100 times greater than samples S1, S2, S3 and S8 for any temperature range. In Table **3**, we present the values of ρ at T = 295 K (ρ(295 K)): for example, ρ(295 K) for sample S8 (thickness of 250 nm and transport dominated by APBs) is 10 times smaller than that of sample S9 (thickness of 360 nm and transport dominated by grains boundaries).

From the results presented above, it is clear that the structure of the precursor plays a fundamental role on the resulting magneto-transport properties. While the transport mechanism observed in the
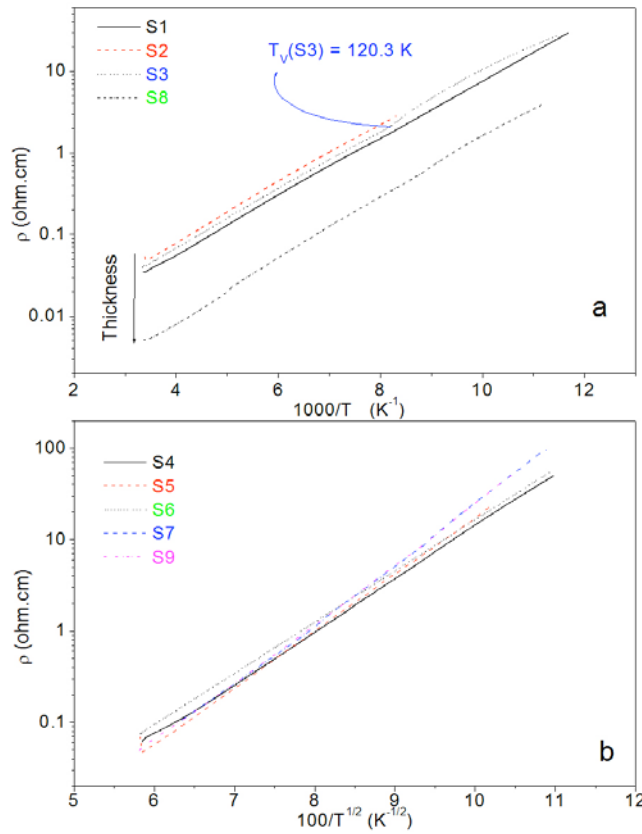
Fig. (7). Fig. (**7a**) shows the plot of $\ln(\rho(T))$ *vs.* $1/T$ for samples S1, S2 and S3 (deposited from precursor $[Fe^{II}Fe^{III}_2(OBu^t)_8]$ at 363 K) and sample S8 (precursor $[Fe^{II}Fe^{III}_2(OBu^t)_8]$ at 357 K on MgO). Fig. (**7b**) shows the curves $\ln(\rho(T))$ *vs.* $1/T^2$ curves of samples S4, S5 and S6 (deposited from precursor $[Fe^{III}_2(OBu^t)_6]$ at 354 K), and samples S7 and S9 (precursor precursor $[Fe^{II}Fe^{III}_2(OBu^t)_8]$ at 357 K on $MgAl_2O_4$ and on Al_2O_3, respectively).

S1, S2 and S3 group (i.e., those from the precursor $[Fe^{II}Fe^{III}_2(OBu^t)_8]$ and $T_{pre}=$ 363 K) was dominated by APB´s, those films from the S2, S3 and S4 group (precursor $[Fe^{III}_2(OBu^t)_6]$ and $T_{pre}=$ 354 K) presented a transport behaviour dominated by grains boundaries. The precursor temperature T_{pre} also present some influence, since group (S7,S8,S9, from precursor $[Fe^{II}Fe^{III}_2(OBu^t)_8]$ and $T_{pre}=$ 357 K) present both mechanisms: for sample S8 (on MgO) the APB´s are dominant while in samples S7 ($MgAl_2O_4$) and S9 (Al_2O_3) the grains boundaries dominate the transport phenomenon. This analysis agree with the pointed out above concerning the MFM images of the films.

All samples presented a similar dependence of the resistivity with the applied field (MR(H) curve, obtained according eq. (1)), as shown in Fig. (**8a**) and (**8b**) for the in-plane and out-of-plane measurements, respectively. The MR value at 1592 kA/m in the in-plane configuration varies from 1.7 % for sample S1 up to 3.6 % for sample S8. For the out-of-plane configuration, we observe that the values are slightly smaller: 1.4 % and 3.1 % for sample S1 and S8, as shown in Table **3**. In the low field region (H < 398 kA/m), in-plane and out-of-plane MR(H) curves present linear and parabolic behaviour, respectively, while for H < 795 kA/m both curves shown a linear behaviour. This difference in the MR(H) curves at low-fields was observed in both polycrystalline [6,18,30] and epitaxial [17,29] films. For polycrystalline films, the linear and quadratic behaviour at low fields for in-plane and out-of-plane curves can be explained in terms of the tunnelling of the spin-polarized electrons through inter-grain anti-ferromagnetic boundaries [18]. In epitaxial films, these behaviours at low-fields can be explained in terms of a model

based in the APBs and uniaxial anisotropy proposed by Eerenstein *et al* [29]. According to this model, the transport properties in the epitaxial Fe_3O_4 films are determined by the tunnelling of spin-polarized electrons through the thin and marked APBs (anti-ferromagnetic domain boundaries), adding the effects of a uniaxial anisotropy constant K for low applied fields. The conductivity σ for this kind of system calculated for a non-adiabatic limit is given proportional to t^2 α $cos^2\varphi_{AF}$, where t^2 is the transfer integral and φ_{AF}, is the angle between the moments in the antiferromagnetic boundary. The inclusion of the uniaxial anisotropy field (H_{AN}) defines two distinct regimes for $cos^2\varphi_{AF}$:

$$cos^2\varphi_{AF} = \frac{(M_s H)^2}{K}; H < H_{an}$$

$$cos^2\varphi_{AF} M_s H = K; H > H_{an}. \qquad \text{eq. (3)}$$

Expanding the (field-independent) conductivity of bulk material in powers of a field-dependent term $\sigma_{AF}(H)$ (small perturbations), we obtain a field-dependent magnetoresistance given by:

$$MR(H) = \frac{\rho_H - \rho_0}{\rho_0} = \left(\frac{d\sigma}{d\sigma_{AF}}\right)_0 \frac{d\sigma_{AF}}{\rho_0} \qquad \text{eq. (4)}$$

Therefore, in-plane and out-of-plane MR(H) curves must scale with the respective magnetization curves, in this case $(M/M_S)^2$ *vs.* H, for the low-field region. Fig. (**9**) shows that the scaling between these curves is excellent for sample S8. In the high-field region (H > 795 kA/m) where the magnetization is almost saturated, the conductivity showed a linear dependence of the applied field.

As the grain-boundaries act as scattering centers for the antiferromagnetically-coupled spin-polarized electrons, it is expected that samples S4, S5, S6, S7 and S9 display MR(H) curves that are similar to those measured for samples S1, S2, S3, and S8. Therefore, the samples where the grains boundaries or APBs dominate the trasnport properties will have different thermal dependence of the resistivity, but similar MH(H) curves.

Sample S7, S8 and S9 presented the largest MR values as consequence of their synthesis conditions. The higher MR values observed for this set of samples could be associated with the larger density of APBs or grain-boundaries, depending of the sample, which was in turn originated from the faster growth rate observed for these samples. The different (faster) kinetics is likely to produce an increment of the "seed" magnetite islands during the first stages of the deposition. Consequently, it could lead to an increment in the density of APBs and grain-boundaries, which is also reflected in the magnetic properties of the system, specifically in the temperature of the reduction in the magnetization as consequence of the Verwey transition (Fig. **4**).

It is interesting to note the deviations observed in the contents of Fe and O with respect to the quantities expected for magnetite (relation Fe/O = 0.75), obtained from RBS data in these films. Indeed, for sample S2 and S7, the amount of Fe/O are 0.61 and 0.64, close to the value expected for maghemite (0.66). Although the presence of small amounts of maghemite could not be completely ruled out by the present data, it is worth to mention that the errors involved in RBS measurements and analysis (~ 5 %) could at least partially explain this deviation. However, the electrical behaviour of both gamma-Fe2O3 and Fe4O4 phases are completely different one from another. Maghemite is an insulator with resistivity values several orders of magnitude larger than those usually found for magnetite at room temperature. In our samples, the resistivity measured varied from 5 to 75 mΩ.cm, whereas maghemite values are usually within the 30 kΩ.cm range. Additionally, the films presented a clear Verwey transition, a signature og magnetite that is not present in maghemite. It is interesting to mention that the magnetotransport effects observed for both mechanisms, AF-APBs and
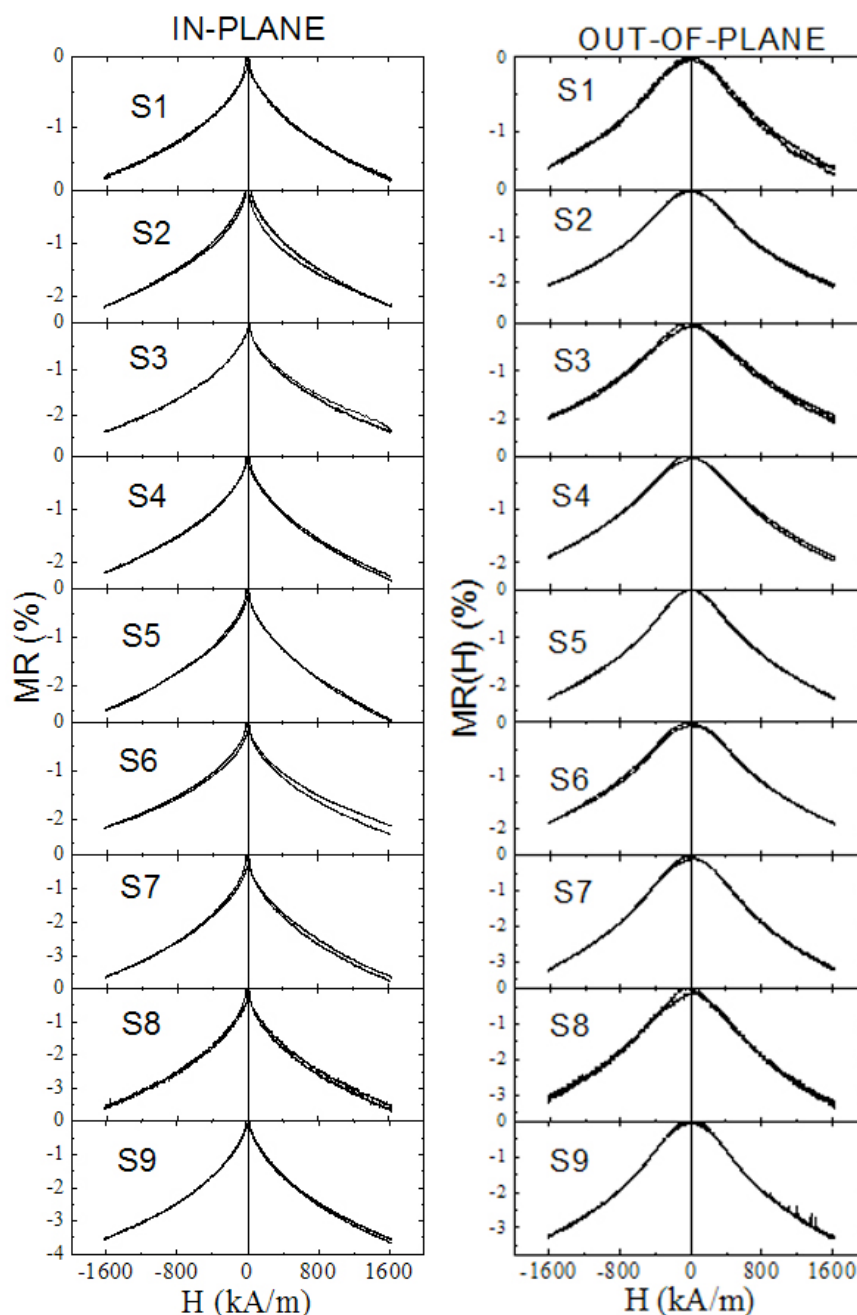
Fig. (8). Fig. (**8a**) and (**8b**) present the magneto-resistance curves with the applied field up to 1592 kA/m (MR(H), obtained according eq. (1)) for the in-plane and out-of-plane measurements, respectively, of all samples.

grain-boundary-scattering, are not expected for insulating systems such as maghemite. The above data make the possibility of maghemite to be present highly unlikely.

4 – CONCLUSIONS

The first conclusion from the systematic analysis of the present series of magnetite films is the strong influence of the precursor type and temperature on both the resulting microstructural and magneto-transport properties. Regarding the $[Fe^{II}Fe^{III}_2(OBu^t)_8]$ precursor, the presence of both Fe(II) and Fe(III) centers in a single framework resulted in Fe_3O_4 films with higher M_S and lower saturation field than those deposited from $[Fe^{III}_2(OBu^t)_6]$ precursor. By appropriate combination of the precursor kind, substrate and deposition temperatures T_{pre}, the observed scattering was dominated by either APB´s or grain boundaries. These results confirm the possibility to tune the magnetic and transport properties of magnetite films from CVD deposition by selecting appropriate deposition temperature and precursor type.
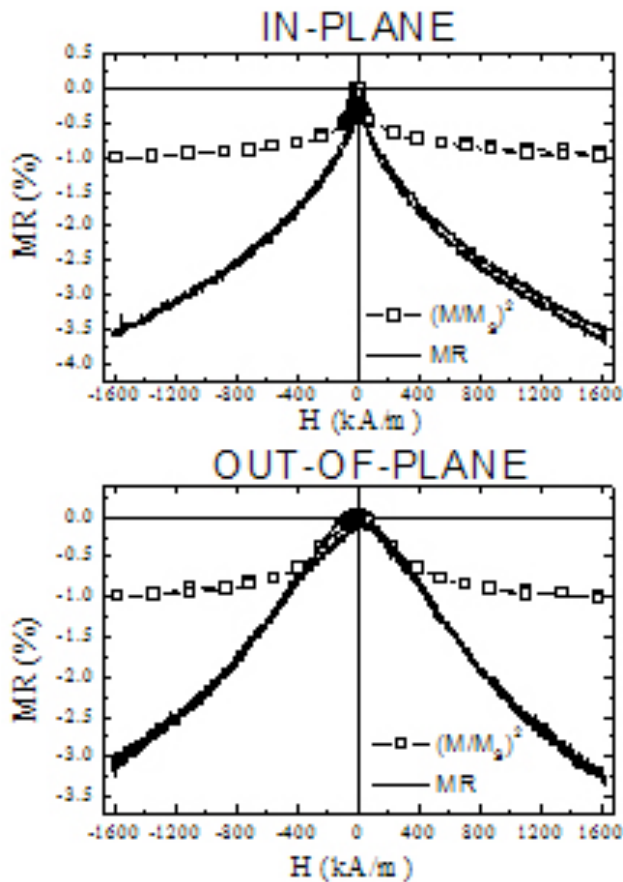
CONFLICT OF INTEREST

The authors confirm that this article content has no conflicts of interest.

Table 3.   **Resistivity ρ(T) and magnetoresistance MR(H) parameters for each sample. The activation energy E_a and resistivity $ρ_0$ were obtained from the linear fitting of ρ(T) curves using eq. (2); ρ(295 K) and MR(2T) were obtained directly from MR(H) curves**

Sample	Transport Mechanism	E_a (meV)	$ρ_0$ (mΩ.cm)	ρ(295 K) (mΩ.cm)	MR(2 T) % In-Plane	MR(2 T) % Out-Plane
S1	APB's	70	2.2	35.1	-1.7	-1.4
S2	APB's	72	2.9	53.2	-2.0	-2.0
S3	APB's	71	2.5	42.4	-2.1	-1.8
S4	Grain boundaries	-	-	61.3	-2.2	-1.8
S5	Grain boundaries	-	-	69.4	-2.2	-2.2
S6	Grain boundaries	-	-	75.3	-2.2	-1.8
S7	Grain boundaries	-	-	63.1	-3.3	-3.4
S8	APB's	75.5	0.3	5.2	-3.6	-3.2
S9	Grain boundaries	-	-	49.8	-3.5	-2.9

Fig. (9). MR(H) and $(M/M_S)^2$ *vs* H curves of sample S8 in the in-plane and out-of-plane measurements.

ABREVIATIONS

E_a	=	Activation Energy
$φ_{AF}$	=	Angle Between Magnetic Moments in the Antiferromagnetic Boundary
AF-APB	=	Antiferromagnetic Antiphase Boundaries
APB	=	Antiphase Boundaries
H	=	Applied Field
AFM	=	Atomic Force Microscope
CVD	=	Chemical Vapor Deposition
H_C	=	Coercive Field
T_C	=	Curie Temperature
I	=	Current
DPT	=	Deposition Time
FC	=	Field-Cooling
FWHM	=	Full Width at Half Maximum
MFM	=	Magnetic Force Microscopy
M	=	Magnetization
MR	=	Magnetoresistance
MBE	=	Molecular Beam Epitaxy
T_{pre}	=	Precursor Temperature
PLD	=	Pulsed Laser Deposition
ρ	=	Resistivity
rms	=	Root Mean Square of Surface Roughness
RBS	=	Rutherford Backscattering Spectroscopy
M_S	=	Saturation Magnetization
T_{sub}	=	Substrate Temperature
T_V	=	Temperature of Verwey Transition
d	=	Thickness of the Film

H_{AN}	=	Uniaxial Anisotropy Field
V	=	Voltage
δT_V	=	Width of Verwey Transition
XRD	=	X-ray Diffraction
ZFC	=	Zero-Field-Cooling

REFERENCES

[1]   Bauminger, R; Cohen, S.G.; Marinov, A.; Ofer, S; Segal, E. *Phys. Rev.*, **1961**, *122*, 1447.

[2]   Ziese, M.; Blythe, H.J.J. Phys.: *Condens. Matter*, **2000**, *12*, 3.

[3]   Ziese, M. *Rep. Prog. Phys.*, **2002**, *65*, 143.

[4]   Ogale, S.B.; Ghosh, K.; Sharma, R.P.; Greene, R.L.; Ramesh, R.; Venkatesan, T. *Phys. Rev. B*, **1998**, *57* 7823.

[5]   Tang, J.; Wang, K.; Zhou, K. *J. Appl. Phys.*, **2001**, *89*, 7690.

[6]   Liu, H.; Jiang, V.; Bai, H.L.; Zheng, R.K.; Wei, H.L.; Zhang, X.X. Appl. Phys. Lett., **2003**, 83, 3531.

[7]   Arora, S.K.; Wu, H.-C.; Yao, H.; Ching, W.Y.; Choudhary, R.J.; Shvets, I.V.; Mryasov, O.N. *IEEE Transactions on Magnets*, **2008**, *44*, 2628.

[8]   Cornell, R.M.; Schwertmann, U. *The Iron Oxides*, Weinheim:Germany, **1996**.

[9]   Li, P.; Jiang, E.Y.; Bai, H.L. *J. Phys. D: Appl. Phys.*, **2010**, *43*, 265002.

[10] Margulies, D.T.; Parker, F.T.; Spada, F.E.; Goldman, R.S.; Li, J.; Sinclair, R.; Berkowitz, A.E. *Phys. Rev. B*, **1996**, *53*, 9175.

[11] Hibma, T.; Voogt, F.C.; Niesen, L.; Van der Heijden, P.A.A.; De Jonge, W.J.; Donkers, J.J.T.M.; Van der Zaag, P.J.*J. Appl. Phys.,* **1991**, *85*, 5291.

[12] Sena, S.P.; Lindley, R.A.; Blythe, H.J.; Sauer, C.H.; Al-Kafarji, M.; Gehring, G.A. *J. Magn. Magn. Mater.*, **1997**, *176*, 111.

[13] Voogt, F.C.; Palstra, T.T.M.; Niesen, L.; Rogojanu, O.C.; James, M.A.; Hibma, T. *Phys. Rev. B*, **1998**, *57*, R8107.

[14] Margulies, T.; Parker, F.T.; Rudee, M.L.; Spada, F.E.; Chapman, J.N.; Aitchison, P.R.; Berkowitz, A.E. *Phys. Rev. Lett*., **1997**, *79*, 5162.

[15] Cheng, J.; Sterbinsky,G.E.; Wessels, B.W. *J. Cryst. Growth*, **2008**, *310*, 3730.

[16] Chen, Y.Z.; Sun, J.R.; Han, Y.N.; Xie, X.Y.; Shen, J.; Rong, C.B.; He, S.L.; Shen, B.G. *J. Appl. Phys.*, **2008**, *103*, 07D703.

[17] Eerenstein, W.; Palstra, T.T.M.; Saxena, S.S.; Hibma, T. *Phys. Rev. Lett.*, **2002**, *88*, 247204.

[18] Mantovan, R.; Lamperti, A.; Georgieva, M.; Tallarida, G.; Fanciulli, M.J. *Phys. D: Appl. Phys.*, **2010**, 43, 065002.

[19] Bohra, M.; Venkataramani, N.; Prasad, S.; Kumar, N.; Misra, D.S.; Sahoo, S C.; Krishnan, R. J. *Magn. Magn. Mater.*, **2007**, *310*, 2242.

[20] Gudavarthy, R.V.; Gorantla, S.; Mu, G.; Kulp, E.A.; Gemming, T.; Eckert, J.; Switzer, J.A. Chem. Mater., **2011**, 23, 2017.

[21] Mathur, S.; Veith, M.; Sivakov, V.; Shen, H.; Huch, V.; Hartmann, U.; Gao, H. *Chem. Vap. Deposition*, **2002**, *8*, 277.

[22] Mathur, S.; Veith, M.; Ruegamer, T.; Hemmer, E.; Shen, H. Chem. Mater., **2004**, 16, 1304.

[23] Cowley, A.H.; Jones, R.A. *Angew. Chem.*, **1989**, *28*, 1208.

[24] Trindade, T.; O'Brien, P.; Pickett, N.L. *Chem. Mater.*, **2000**, *13*, 3843.

[25] Mathur, S.; Shen, H., *Inorganic nanomaterials from molecular templates.* In: *Encyclopedia of Nanoscience and Nanotechnology*, Nalwa, H.S., ed.; American Scientific Publisher, **2004**; pp. 131-191.

[26] Kale, S.; Bhagat, S.M.; Lofland, S.E.; Scabarozi, T.; Ogale, S.B.; Orozco, A.; Shinde, S.R.; Venkatesan, T.; Hannoyer, B.; Mercey, B.; Prellier, W. *Phys. Rev. B*, **2001**, *47*, 205413.

[27] Bollero, A.; Ziese, M.; Höhne, R.; Semmelhack, H.C.; Köhler, U.; Setzer, A.; Esquinazi, P.J. *Magn. Magn. Mater.*, **2005**, *285*, 279.

[28] Reisinger, D.; Majewski, P.; Opel, M.; Alff, L.; Gross, R. *Appl. Phys. Lett.*, **2004**, 85, 4980.

[29] W. Eerenstein, W.; Palstra, T.T.M.; Hibma, T.; Celotto, S. *Phys. Rev. B*, **2002**, *66*, 201101.

[30] Coey, J.M.D.; Berkowitz, A.E.; Balcells, L.; Putris, F.F.; Parker, F.T. *Appl. Phys. Lett.*, **1998**, *72*, 734.